Journal of Operation and Automation in Power Engineering

Vol. 14, No. 2, Apr. 2026, Pages: 131-141

http://joape.uma.ac.ir

Research Paper

Robust Control Design for Voltage and Frequency Fluctuation Control under Substantial Load Variation of Islanded Microgrid System

Oinam Manganleiba Meetei [1, *], *Marimuthu Prakash* [2], and *Rajagopal Kumar* [3]

[1]*Department of Electrical Engineering, Manipur Technical University, Imphal, Manipur- 795004, India.*
[2]*Department of Electrical and Electronics Engineering, National Institute of Technology, Nagaland, Chumukeidma- 797103, India.*
[3]*Department of Electronics and Instrumentation Engineering, National Institute of Technology, Nagaland, Chumukeidma- 797103, India.*

Abstract— *The use of standalone microgrids is rapidly increasing due to their advantages in terms of environmental, economic, and technical aspects. However, the microgrid is vulnerable to frequency and voltage oscillation because of its separation from the main grid, the uncertainties of loads, and the use of uncertain renewable energy sources such as wind and solar energy. Therefore, the need for a dynamic controller arises to regulate voltage and frequency. This paper presents Double Integral Sliding Mode Control (DISMC) and Artificial Neural Network (ANN) based on the Feed Forward Bayesian Regularization (FF-BR) algorithm. DISMC is developed to control voltage and steady-state error. The ANN based on the FF-BR algorithm is adapted to regulate the current. These controllers enhance the performance of droop control for inverter base Distributed Generation (DG) units in an islanded microgrid system. The controllers are designed based on the islanded microgrid dynamic model and load variations. The suggested control algorithm is implemented in Matlab/Simulink. The performance of the controller is evaluated under variable loads and uncertainties. The results are then compared with droop control with the Proportionate Integral (PI) controller. The performance of the proposed controllers is seen to outdo the existing PI method in the regulation of voltage and frequency.*

Keywords—Distributed generation, double integral sliding mode control, droop control, bayesian regularization, photo voltaic.

1. INTRODUCTION

The traditional centralized generation of electric power networks encounters energy loss and higher monetary investment due to long-distance transmission. It is being replaced by a distributed generation (DG) electric power network based on renewable energy sources and energy storage technologies. The DG electric power network is more flexible and advantageous. If integrated with a low/medium local grid network, their reliability can be further enhanced [1]. However, while doing so, the DG electric power network encounters frequency and voltage fluctuation. This is brought about by the unpredictable nature of renewable energy generation patterns [2]. This issue can be solved by controlling the interdependent power electronic converters. In addition, the filter and controller characteristics of the DG electric power network are to be selected carefully [3].

The DG unit controllers are required to manage the voltage and frequency level of the electric power network. They should also be able to supply total active and reactive powers to the loads in autonomous mode [4]. However, voltage and frequency regulation in grid-connected and islanded modes has been pointed out as two major challenges in DG electric power networks namely microgrid operation and control [5]. The voltage and frequency are stabilized in various traditional and advanced ways [6]. A multi-stage frequency regulation in an isolated microgrid is designed [7]. The microgrid (MG's) voltage and frequency control can be achieved through local control loops. In doing so, circulating currents between parallel inverters are often avoided using control methods based on droop characteristics. The droop control mechanism is unable to regulate the nominal voltage and frequency. A secondary control mechanism based on the sliding-mode technique is used to address the problems with droop control [8]. Here, the controller maintains unregulated fluctuations at the master layer within allowable limits for any variation in generation and loading pattern [9]. The presence of external disturbances in an islanded microgrid causes voltage and frequency fluctuation. A full-order sliding-mode (FOSM) control approach is used to mitigate such fluctuations [10].

The use of centralized secondary control is often suggested for islanded microgrids. It maintains the right distribution of reactive power while restoring voltage and frequency anomalies. Various methods such as SMC-based distributed cooperative control [11] and a Neural network-based model [12] are implemented to address voltage and frequency disruptions. Artificial Neural Network (ANN) and Genetic Algorithm (GA) were also used to regulate the voltage and frequency changes at the secondary layer

Received: 25 Mar. 2024
Revised: 24 May 2024
Accepted: 01 Jun. 2024
*Corresponding author:
E-mail: mangal.oinam@gmail.com (O.M. Meetei)
DOI: 10.22098/joape.2024.14841.2136

[13]. GA optimization makes parameter initialization possible, and ANN enables real-time parameter tuning and quicker system dynamics prediction. A multi-agent system's noise-resilient cooperative secondary control has been proposed by researchers [14]. It considers both noisy measurements and the system's comprehensive non-linear model. These methods can be verified for hybrid or DC microgrid structures. The suggested control technique restores the voltage and frequency changes in minor and significant signal disturbances.

Control of system secondary frequency using the adaptive Deep Reinforcement Learning (DRL) method is presented [15]. In this study, the tidal energy generation and vehicle-to-grid integration units were taken into account in an isolated microgrid. This approach manages frequency while controlling any load disturbances and power fluctuations. A secondary controller based on data-driven heuristic dynamic programming is shown [16]. The suggested framework swiftly adjusts frequency while ensuring accurate active power sharing across all distributed energy resources (DERs). It is well adapted to load disturbances. By studying the articles written on effective controlling of Islanded microgrid control, the listed problems are observed:

- In a massive load disturbance, the frequency oscillation is above the acceptable range [17, 18].
- In most of the papers, the effect caused by the variable power generation with variable load disturbances is less, and hence the controller can easily track and dampen the oscillations [19, 20].
- To the best of the writer's understanding, SMC is implemented in microgrid parameters control [21, 22]. Whereas the implementation of a combination of controllers (DISMC, droop control, and FFBR) for the stabilization issues of microgrid has not been performed.

This paper presents the implementation of an actual model of energy sources in the MG. Despite the variation in the output power of renewable energy sources, the proposed droop control with DISMC and ANN-BR controllers can supply the standard voltage and frequency. The proposed model consisting of medium to high load changes is tested using the Simpower system toolbox of Matlab. The simulation results are provided to confirm the effectiveness of the suggested controller. The primary goal of this effort is described as:

- Removal of chattering effect caused by undesired dynamics and unpredictable loads.
- Design of control algorithm with the combination of intelligent control.
- Integration and interoperability of variable power sources and supplies steady state power to consumers.

This paper demonstrates how renewable energy sources are designed in Section 2. The dynamic model equations for the design are described in Section 3. Droop control with proposed control methods is explained in Section 4. Section 5 displays the results of the simulation and compares the outcomes with the suggested controller. Section 6 concludes with a final statement.

2. Configuration of Islanded Microgrid

Fig. 1 depicts the suggested simulation microgrid model. It comprises various energy sources such as wind power generation, photo voltaic (PV) array, fuel cell, and battery. Each converter unit's energy source is a parallel combination of two green energy sources. Converter 1 energy source is the combination of a wind turbine and BESS. The same applies to converter 2 PV and wind turbine, and converter 3 fuel cell and BESS. All the converting units of DGs are synchronously working. The energy produced from green energy sources fluctuates. There is a necessity for effective control techniques for reliable output power generation. To maximize power generation, renewable energy sources must be designed and managed. To extract power efficiently, a DC/DC converter is equipped with a Maximum Power Point Tracking (MPPT) controller. The converted power is supplied to the Point of Common Coupling (PCC) via a coupling transformer. The power that is converted from DC to AC is integrated at PCC to maximize the load-bearing capability. The two similar DG units, designated DG1 and DG2 are integrated through a transmission line. The time-varying loads are connected through the PCC.

2.1. Modeling of PV system

PV-based solar energy is freely available from nature. It is available abundantly and also environment friendly. PV solar energy is replenishable and non-exhaustive. A major drawback of this system is the inefficiency of capturing solar energy. This work uses a single diode to create a PV system. The design expression for the output current (I_{ov}) and the photocurrent (I_{is}) are given in [23, 24].

The PV system model consists of 15 module strings and 190 parallel strings. The PV is designed for 300KW. Fig. 2 displays the PV system's Maximum Power Point Tracking (MPPT) control diagram, which is based on sliding mode control (SMC). The maximum power is tracked by comparing voltage, current, and power with predefined values. The overall error signal is sent to generate a pulse-wide modulation (PWM) signal. The sliding mode control law is expressed as:

$$\text{Sliding surface,}\quad s = (P - P_{\text{ref}}) / (I - I_{\text{ref}}) \tag{1}$$

where I represents the output current P represents the power output.

$$\text{Control law} = |s|^{0.9} sign\,(s) + \alpha_1\,(e_\delta / V_o) - V/V_o \tag{2}$$

where V is the output voltage and $e_\delta = \delta_{err}/\delta$.

2.2. Wind turbine characteristics

Wind energy is a cost-effective form of power source compared to traditional energy sources. This paper uses wind energy as a second DG unit wherein the rectified output voltage is connected to the DC-DC boost converter. The generator rotor is powered by the conversion of wind energy into mechanical energy by a wind turbine. A mechanical actuator often adjusts a variable-speed wind turbine's blade pitch angle [25].

It highlights the importance of the pitch angle controller. It also consists of a wind turbine with variable speed that is pitch-regulated. The wind turbine system's SMC base MPPT control diagram is shown in Fig. 3 and control parameters are given in Table 1. Voltage and current error signals are redirected to the PWM signal generator. The latter is used to generate an accurate signal for regulating the DC voltage. The SMC controllers to regulate DC voltage are expressed as:

$$\dot{x}\,(t) = v - v_{\text{ref}} \tag{3}$$

The sliding surface definition is expressed as:

$$S = x\,(t) + G\dot{x}(t) \tag{4}$$

where G is the +ve gain.

$$\text{Control law u} = \dot{x}(t) + \beta |s|^{\beta sign(s)} \tag{5}$$

where β is the sliding gain.

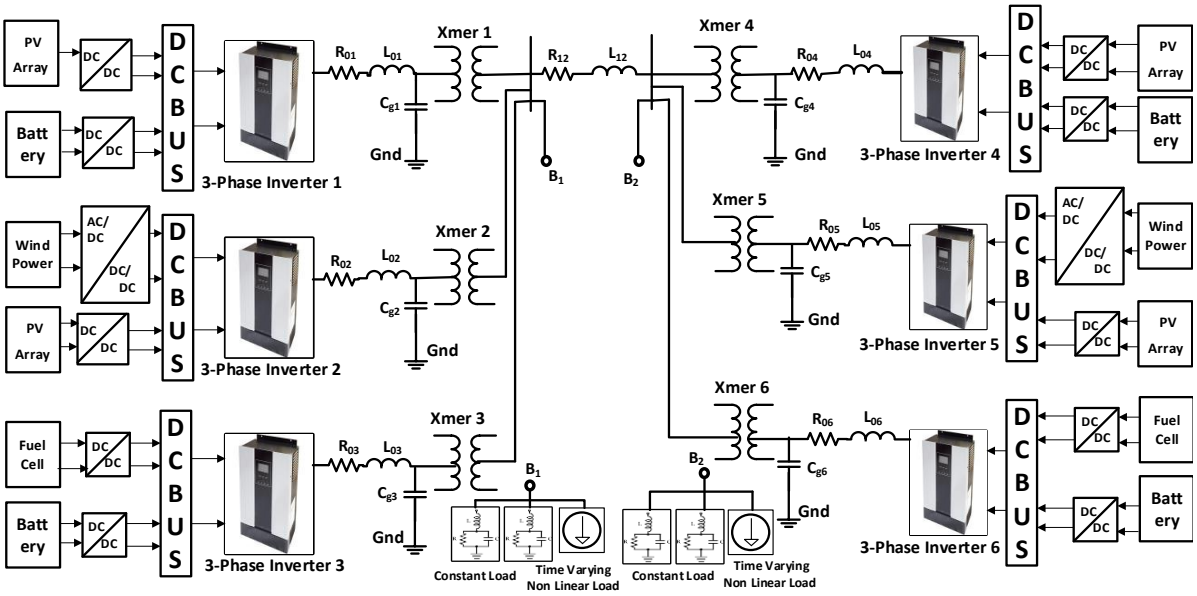

Fig. 1. The suggested islanded micro-grid system.

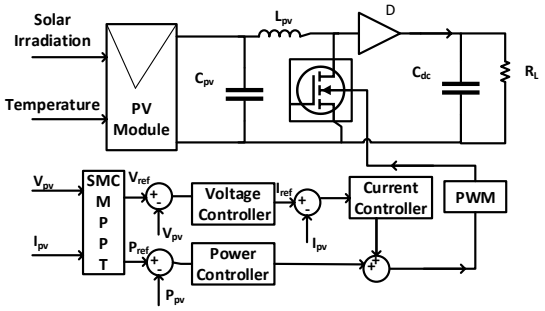

Fig. 2. MPPT control of PV module using SMC.

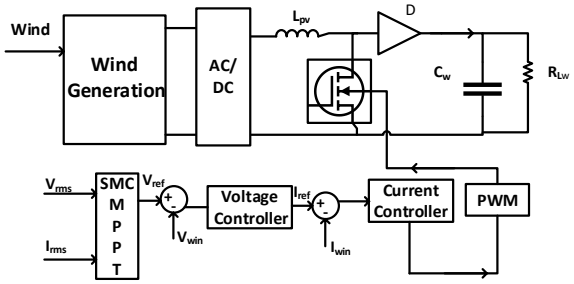

Fig. 3. MPPT control of wind turbine using SMC.

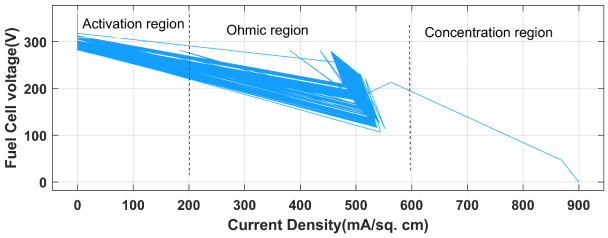

Fig. 4. Fuel cell polarization curve.

2.3. Fuel cell characteristics

Fuel Cell (FC) has the characteristics of robust reliability. It can work in hazardous environments with zero emissions. Therefore, it can be used for cogeneration purposes with increased power and improved efficiency by converting heat generated to electricity. It is also the best-suited energy source for DG applications. The validated dynamic model equations serve as the foundation for the FC model [26], and it is used to develop an 80kW system. It is a self-contained model that runs under constant channel pressure. This model generates a polarization curve that shows the typical voltage losses against the current density in an FC as illustrated in Fig. 4. There are three regions that these characteristics curve can be divided into: the activation region, the ohmic region, and the concentration region. A voltage dip across the FC occurs due to the activation loss inside the FC. The ohmic loss in the FC stack causes the voltage to fall in the middle of the curve. As the load current increases, concentration loss will cause the output voltage at the curve to drop significantly [27].

3. DYNAMIC MODEL OF STUDY SYSTEM

The system dynamic model equations with reference to [28] are defined as follows. The definition of phase voltage output is:

$$V_{oi} = V_{Li} - L_{oi}d/dtI_{oi} - R_{oi}I_{oi} = M_iV_{dci}/2 \qquad i = 1, 2, 3 \tag{6}$$

where V_{Li}, I_{oi}, M_i, and V_{dci} represent the load voltage, phase current, modulation index of converters, and DC bus voltage respectively. R_{oi} and L_{oi} represent transmission line resistance and inductance of DGi respectively.

For the linear loads, the voltage equation is stated by:

$$V_{Li} = R_{Li}I_{Li} + L_{Li}d/dtI_{Li} \tag{7}$$

where I_{Li}, R_{Li}, and L_{Li} represent phase current, resistance, and inductance of linear load respectively.

A varying load's real and reactive capacities are expressed as:

$$P_{\text{ivar}} = P_{io}(V_{oi}/V_n)^2(f_{oi}/f_n)^2 \tag{8}$$

Table 1. Active and reactive power load variation scenario.

Parameters	Values and Unit
AC voltage	440V (L-G)
Nominal frequency	50Hz
Nominal battery voltage	720V
Battery capacity	100Ah
Initial state of charge(%)	100
Wind turbine-rated power	10kW
The total power rating of the PV array	300kW
Irradiance level	600-1000W/m^2
Fuel Cell rating	20kW
Dc bus voltage	820V
Transformer winding 1 and 2 parameters	
Winding resistance,	0.0016 R(pu)
Winding inductance	0.02 L(pu)
Magnetization resistance	201 R_m(pu)
Magnetization inductance	201 L_m(pu)
Nominal ratings, s	450kVA
Voltage ratio	480/440
Transmission line parameters	
Positive sequence resistance	0.01274Ω/km
Zero sequence resistance	0.3865Ω/km
Positive sequence inductance	0.9338mH/km
Zero sequence inductance	4.1262mH/km
Positive sequence capacitance	11.72x 10^{-9}F/km
Zero sequence capacitance	8.752x10^{-9}mH/km
Constant loads	
Real power(kW)	350
Reactive power(kVar)	100
DISMC gains	
α_1,α_2,α_3,α_4 and δ	1.05,0.3,0.01,1.5 and 0.2
PI controller gains	
K_p and K_i	0.1 and 7

Parameters	Values and unit
AC voltage	440V (L-G)
Nominal frequency	50Hz
Nominal battery voltage	720V
Battery capacity	100Ah
Initial state of charge(%)	100
Wind turbine-rated power	10kW
The total power rating of PV array	300kW
Irradiance level	600-1000W/m^2
Fuel Cell rating	20kW
Dc bus voltage	820V
Transformer Winding 1 and 2 parameters	
Winding resistance,	0.0016 R(pu)
Winding inductance	0.02 L(pu)
Magnetization resistance	201 R_m(pu)
Magnetization inductance	201 L_m(pu)
Nominal ratings, s	450kVA
Voltage ratio	480/440
Transmission line parameters	
Positive sequence resistance	0.01274Ω/km
Zero sequence resistance	0.3865Ω/km
Positive sequence inductance	0.9338mH/km
Zero sequence inductance	4.1262 mH/km
Positive sequence capacitance	11.72x10^{-9}F/km
Zero Sequence Capacitance	8.752x10^{-9}mH/km
Constant loads	
Real power(kW)	350
Reactive power(kVar)	100
DISMC gains	
α_1,α_2,α_3,α_4 and δ	1.05,0.3,0.01,1.5 and 0.2
PI controller gains	
K_p and K_i	0.1 and 7

$$Q_{\text{ivar}} = Q_{io}(V_{oi}/V_n)^2(f_{oi}/f_n)^2 \tag{9}$$

where P_{io} and Q_{io} represent the base active and reactive powers, f_{oi} is the frequency, V_n and f_n represent the system's nominal voltage and frequency.

d-q axis reference frame for voltage and variable load current equations are as follows:

$$\begin{bmatrix} V_{oiq} \\ V_{oid} \end{bmatrix} = \begin{bmatrix} 1 & -d/dtI_{oiq} \\ 1 & -d/dtI_{oid} \end{bmatrix} \begin{bmatrix} V_{Liq} & V_{Lid} \\ L_{oi} & L_{oi} \end{bmatrix} + \begin{bmatrix} -I_{oiq} & -\omega_{oi}I_{oid} \\ -I_{oid} & -\omega_{oi}I_{oiq} \end{bmatrix} \begin{bmatrix} R_{oi} & R_{oi} \\ L_{oi} & L_{oi} \end{bmatrix} = \begin{bmatrix} M_{iq} & V_{dci}/2 \\ M_{id} & V_{dci}/2 \end{bmatrix} \tag{10}$$

d-q axis variable load current is expressed by the following equations:

$$I_{ivarq}(t) = 2/3\left((P_{ivar}V_{Liq} - Q_{ivar}V_{Lid})/\left({V_{Liq}}^2 + {V_{Lid}}^2\right)\right) \tag{11}$$

$$I_{ivard}(t) = 2/3\left((P_{ivar}V_{Lid} - Q_{ivar}V_{Liq})/\left({V_{Liq}}^2 + {V_{Lid}}^2\right)\right) \tag{12}$$

The converter's d-q axis reference output current is described as:

$$I_{oiq}* = \sigma I_{iq} + I_{ijq} + I_{Liq} + I_{iq} + I_{ivarq} + {}_{oi}C_{di}V_{Lid} \tag{13}$$

$$I_{oid}* = \sigma I_{id} + I_{ijd} + I_{Lid} + I_{id} + I_{ivard} - {}_{oi}C_{di}V_{Liq} \tag{14}$$

where C_{di} is capacitor voltages.

4. CONTROL STRATEGIES

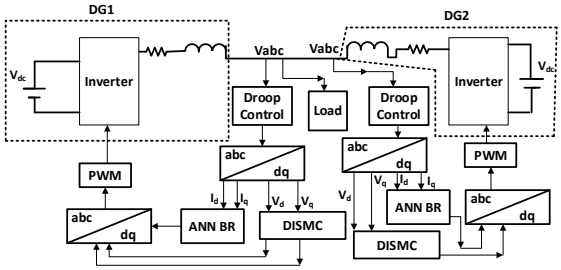

Fig. 5. Control sequence of the proposed system.

The microgrid operates independently. Each DG unit's microgrid frequency and voltage should maintain a standard value. The controllers used in DG units must possess dynamic properties. The main characteristic of the controller is the capability to adjust the parameters. The controller consists of three main parts. They are droop control, voltage control, and current control. The controlling sequence is illustrated in Fig. 5. The output parameters are fed to the droop control for regulating power sharing. Then the signal is converted to a dq reference frame. The separated d and q signals are sent to the current controller and voltage controller. The control signal is sent to the inverter through the PWM signal generator to correct the errors. The modelling of controllers is discussed as follows.

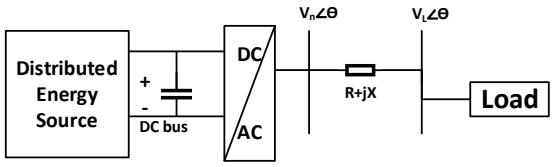

Fig. 6. Distributed energy source with the inverter connected to load.

4.1. Generalized droop control

Droop control is used to govern power-sharing, voltage, and frequency. A DG unit including the inverter is depicted in Fig. 6. The active and reactive power flow expression at point V_n with refer to [29] is shown as:

$$P = \frac{V_n^2}{Z} cos\theta - \ V_n \frac{V_L}{Z} \cos\left(\theta + \delta\right) \tag{15}$$

$$Q = \frac{V_n^2}{Z} sin\theta - \ V_n \frac{V_L}{Z} \sin\left(\theta + \delta\right) \tag{16}$$

where the expression $Z = R + jX$ represents the line impedance.

The microgrid frequency can be adjusted by controlling the real power and the reactive power is used to regulate the voltage [30]. Systems frequency and voltage magnitude with regard to active and reactive power can be expressed as:

$$f = {f_o}^* - \alpha_p \left(P - P_o\right) \tag{17}$$

$$V = V_n - -\alpha_q \left(Q - Q_o\right) \tag{18}$$

where ${f_o}^*$ is the reference frequency.

Here, the microgrid is unable to provide the required real and reactive power when certain load variation occurs. A new approach is explained in the next section to improve the performance.

4.2. d-axis DISMC voltage controller design

Let V_{oid}^* is the reference direct axis voltage. The direct voltage error is defined as:

$$y(t) = V_{oid}^*\left(t\right) - V_d(t) \tag{19}$$

Then, the equation for the double integral sliding surface is defined as [31]:

$$\begin{aligned} sd(t) = k_1 y(t) + k_2 \textstyle\int_0^t y\left(t\right) dt + \\ k_3 \textstyle\iint_0^t y(t) dt dt + \dot{y}(t) \end{aligned} \tag{20}$$

where k_1, k_2 and k_3 are the positive constants.

The inclusion of the integral term $\int_0^t y\left(t\right) dt$ can significantly enhance the performance of the system's steady-state control.

Calculating the derivative of $s_d(t)$ with regard to time.

$$\begin{aligned} \dot{s_d}(t) = k_1 \dot{y}(t) + k_2 y(t) + \\ k_3 \textstyle\int_0^t y\left(t\right) dt + \ddot{y}(t) \end{aligned} \tag{21}$$

Theorem. 1 Let α_1, α_2, α_3, α_4 > 0 and $s_d(t) = 0$ in Eq. (20), is represented in Fig. 7, then the control law is defined as:

$$\begin{aligned} u_d\left(t\right) = \alpha_1 \dot{y}\left(t\right) - \alpha_2 V_{oid}^*\left(t\right) - \alpha_3 \dot{V}_d\left(t\right) + \\ \alpha_4 \textstyle\iint_0^t y(t) dt dt + \delta sat(s\left(t\right)) \end{aligned} \tag{22}$$

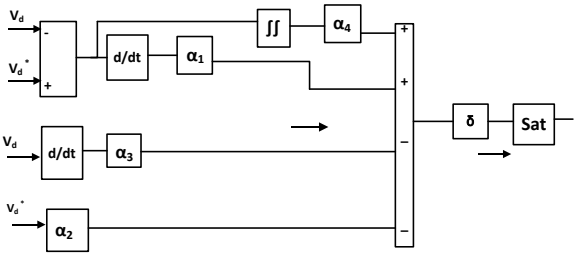

Fig. 7. d-axis voltage control unit of DISMC.

where sat $\left(s_d\left(t\right)/\phi_s\right) =$

$$\begin{cases} 1 & s_d\left(t\right) > \phi_s \\ s_d\left(t\right)/\phi_s & \left|s_d\left(t\right)\right| \le \phi_s \\ -1 & s_d\left(t\right) < \phi_s \end{cases}$$

where Φ_s is the sliding layer, δ and Φ_s are chosen through trial and error to minimize chattering and achieve control accuracy. The asymptotic convergence of the sliding surface is made possible by including the integral term.

Proof. The system of two first-order equations can be used to state the Eqs. ((19) and (22)) equivalently as follows:

$$\begin{cases} \dot{x}_1 = x_2 + \alpha_1 \dot{y}(x_1) - \alpha_2 V_{\text{oid}}^*\left(x_1\right) - \alpha_3 \dot{V}_q\left(x_1\right) \\ \dot{x}_2 = \alpha_4 \int_0^t y(t) dt + \delta \text{sat}(s(x_1)) \end{cases} \tag{23}$$

$$\text{where } x_1 = t,\ x_2 = \alpha_4 \iint_0^t y(t) dt + \delta sat(s\left(t\right))$$

Let a Lyapunov function candidate be then the following equation is obtained:

$$V(x_1, x_2) = \frac{x_2^2}{2} + \alpha_4 \int \int_0^{x_1} y(z) dz + \delta sat(s(z)) \tag{24}$$

$V(x) > 0$, if $x \in R^2 \backslash \{0\}$, then the Lyapunov function derivative will be as:

$$\begin{aligned} &\dot{V} = \\ &\frac{\partial}{\partial x} \begin{bmatrix} x_2 + \alpha_1 \dot{y}(x_1) - \alpha_2 V_{\text{oid}}^*\left(x_1\right) - \alpha_3 \dot{V}_q\left(x_1\right) \\ \alpha_4 \int_0^t y(t) dt + \delta \text{sat}(s(x_1)) \end{bmatrix} = \\ &-\alpha_1 \alpha_2 \alpha_3 \alpha_4 \delta y(t) < 0 \\ &\text{if } x \in R^2 \backslash \{0\} \end{aligned} \tag{25}$$

Applying the La Salle Theorem can therefore be used to demonstrate that x decreases with time increases. The elements of a set $x : \dot{V}\left(x\right) = 0$ are $x_1 = 0$ and x_2 equal to any real number. These values are substituted in Eq. (23). To produce $\dot{x_1} = x_2$, $\dot{x_2} = 0$. Since $x_1 = 0$ instantly implies that $x_2 = 0$, it is simple to demonstrate that the origin is the sole invariant set contained within $x_1 = 0$. So, we established that x_1 and x_2 have asymptotic convergence to zero.

4.3. q-axis DISMC voltage controller design

Let V_{oiq}^* is the reference quadrature axis voltage. The quadrature voltage error is defined as:

$$y(t) = V_{oiq}^*\left(t\right) - V_q(t) \tag{26}$$

Then, the equation for the double integral sliding surface [31] is defined as:

$$Sq(t) = k_1 y(t) + k_2 \int_0^t y\,(t)\,dt + k_3 \int_0^t \int_0^t y\,(t)\,dtdt + \dot{y}(t) \tag{27}$$

where k_1, k_2 and k_3 are the positive constants.

The inclusion of the integral term $\int_0^t y\,(t)\,dt$ can further enhance the system's capability for steady-state control.

Calculating the derivative of $s_d(t)$ with regard to time, we get the following result:

$$\dot{s}_q(t) = k_1 \dot{y}(t) + k_2 y(t) + k_3 \int_0^t y\,(t)\,dt + \ddot{y}(t) \tag{28}$$

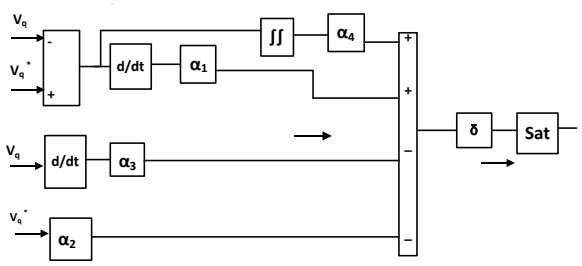

Fig. 8. q-axis voltage control unit of DISMC.

Theorem. 2 Let α_1, α_2, α_3, $\alpha_4 > 0$, $s_q(t) = 0$ in Eq. (27), is represented in Fig. 8, then the control rule can be formulated as:

$$u_q\,(t) = \alpha_1 \dot{y}\,(t) - \alpha_2 V^*_{oiq}(t) - \alpha_3 \dot{V}_q\,(t) + \alpha_4 \iint_0^t y(t)dtdt + \delta sat(s(t)) \tag{29}$$

$$\text{where sat}\,(s_q\,(t)/\phi_s) = \begin{cases} 1 & s_q\,(t) > \phi_s \\ s_q\,(t)/\phi_s & |s_q\,(t)| \le \phi_s \\ -1 & s_q\,(t) < \phi_s \end{cases}$$

where Φ_s is the sliding layer, δ and Φ_s are chosen through trial and error to minimize chattering and achieve control accuracy. The asymptotic convergence of the sliding surface is made possible by the inclusion of the integral term.

Proof. The system of two first-order equations can be used to present the Eqs. (26) and (29) in an equivalent manner in the following equations:

$$\begin{cases} \dot{x}_3 = x_4 + \alpha_1 \dot{y}(x_3) - \alpha_2 V^*_{\text{oid}}\,(x_3) - \alpha_3 \dot{V}_q\,(t) \\ \dot{x}_4 = \alpha_4 \int_0^t y(x_3)dt + \delta \text{sat}(s(x_3)) \end{cases} \tag{30}$$

$$\text{where } x_3 = t,\ x_4 = \alpha_4 \iint_0^t y(t)dtdt + \delta sat(s\,(t))$$

Let a Lyapunov function candidate be as follows:

$$V(x_3, x_4) = \frac{x_4^2}{2} + \alpha_4 \iint_0^{x_3} y(z)dzdz + \delta sat(s\,(z)) \tag{31}$$

$V(x) > 0$, if $x \in R^2 \backslash \{0\}$, then the Lyapunov function derivative will be as follows:

$$\dot{V} = \frac{\partial}{\partial x} \begin{bmatrix} x_2 + \alpha_1 \dot{y}(x_3) - \alpha_2 V^*_{\text{oid}}\,(x_3) - \alpha_3 \dot{V}_q\,(x_3) \\ \alpha_4 \int_0^t y(x_3)dt + \delta \text{sat}(s(x_3)) \end{bmatrix} = -\alpha_1 \alpha_2 \alpha_3 \alpha_4 \delta y(t) < 0 \tag{32}$$

$$\text{if}\, x \in R^2 \backslash \{0\}$$

Applying the La Salle Theorem can therefore be used to demonstrate that x decreases with time. The elements of a set $x : \dot{V}\,(x) = 0$ are $x_3 = 0$ and x_4 equal to any real number. These values are substituted into Eq. (30) to produce $\dot{x_3} = x_4$, $\dot{x_4} = 0$. Since $x_3 = 0$ instantly implies that $x_4 = 0$, it is simple to demonstrate that the origin is the sole invariant set contained within $x_3 = 0$. So, we established that x_3 and x_4 have asymptotic convergence to zero. Also, with the introduction saturation function(boundary layer) and also addition of a double integral term. Discontinuous time derivative will be a continuous integral of its derivative as a result the chattering impact level is decreased.

4.4. Artificial neural networks– feed forward bayesian regularization

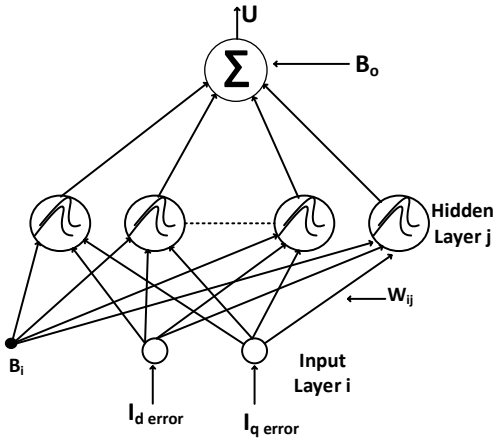

Fig. 9. Structure of ANN-BR.

The d-q axis current control is made by applying a type of ANN. In this, the nodes do not form a cycle of connections in the feed-forward neural network. These networks transfer data without loops or cycles from the input to the output nodes, passing through any hidden nodes in the process [32]. A two-layer neural network is the next most sophisticated neural network. Fig. 9 depicts the ANN with an input layer, two hidden layers, and an output layer. The best quantity of neurons for a hidden layer is established by trial and error. In these systems, the error propagates backward through the system, and the weights and biases are streamlined using a technique called epoch iteration, as shown in Fig. 10. More robustness is offered by feed-forward Bayesian regularized ANNs which may reduce or even do away with the need for time-consuming cross-validation processes. Although this technique takes longer, it may provide strong generalization for complex, small, or noisy datasets [33]. The cost function is defined as:

$$C(w) = \delta \sum_{i=1}^{M_r} [x_i - f(X_i)]^2 + \lambda \sum_{j=1}^{N_p} {w_j}^2 \tag{33}$$

where N_p stands for the weights' number. Concerning the weights w, the cost function, $C(w)$, is minimized given the initial values of the hyper parameters δ and λ. The evidence results are maximized by re-estimation of δ and λ.

The efficiency is achieved using a sigmoid transfer function written as:

$$S_g(x) = f(x) = 1/[1 + \exp(-x)] \tag{34}$$

The expression for the derivative of $f(x)$ is:

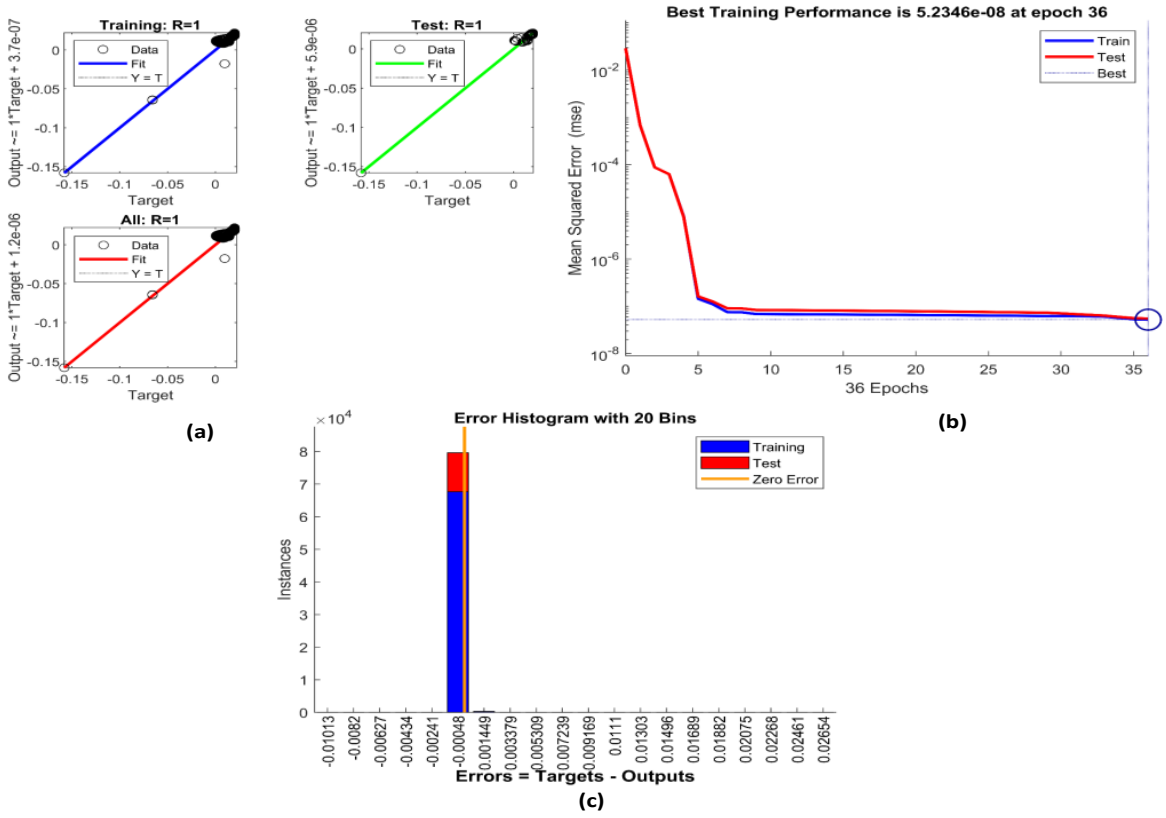

Fig. 10. a) Regression plot of ANN-BR, (b) Training performance plot of ANN-BR, (c) Error histogram plot of ANN-BR.

$$f\prime(x) = f(x)[1 + f(x)] \tag{35}$$

When the squared error in the validation set's prediction reaches its minimum value, the iterations come to an end. Fig. 10-(a,b,c) illustrates the regression, training performance, and error histogram.

Assuming that the probability distributions of the weights and data are Gaussian, the prior probability over the weights, w, can be expressed as follows:

$$(w|\ \delta, H) = (1/K_w(\delta))exp(-\alpha E_w) \tag{36}$$

where error weights.

$$E_w = \sum_{j=1}^{N_p} {w_j}^2$$

The activation function is defined as:

$$\emptyset_h = \frac{2}{1+exp^{(-2*(W_{ij}^{IH}*X_i+B_i^H))}} - 1 \quad for\ ij = 1, 2, 3\ldots \tag{37}$$

5. Results and Discussions

The proposed microgrid model consisting of various renewable energy sources is depicted in Fig. 1. It is designed and simulated in Matlab/Simulink. The system is simulated with varying load scenarios. Fig. 11 and Table 2 depict the active and reactive power load variation scenarios. Table 1 displays the various system and control settings. To assess how well the suggested droop control based on DISMC and ANN-BR performs against the traditional controller droop control with the PI anti-windup method, various

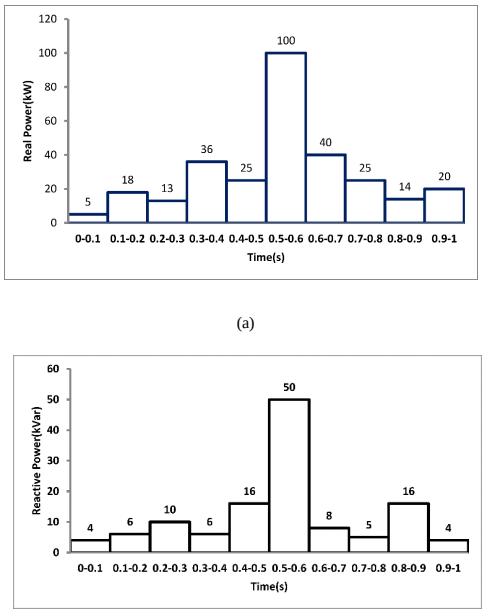

Fig. 11. (a) Real power variation scenario of load, (b) Reactive power variation scenario of load.

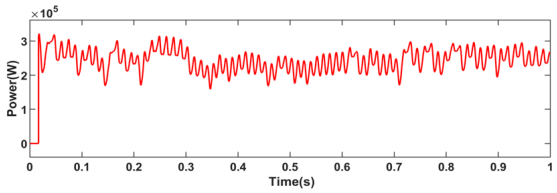

Fig. 12. PV Output power under variable irradiance conditions.

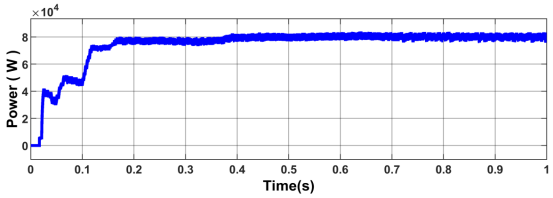

Fig. 13. Power output of wind turbines in varying wind conditions.

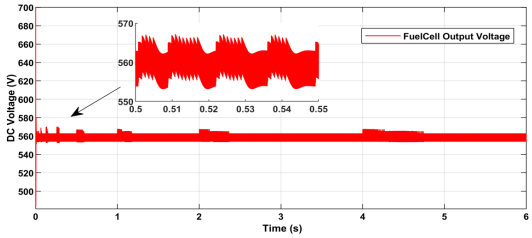

Fig. 14. Fuel cell output voltage.

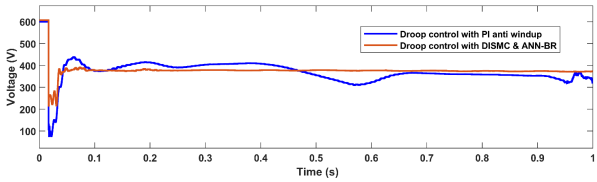

Fig. 15. DG1's output voltage at PCC under various load scenarios.

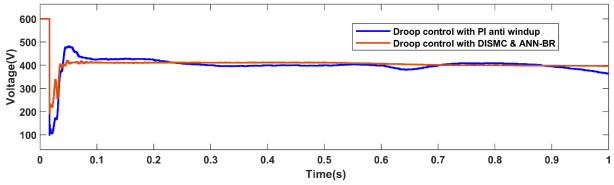

Fig. 16. DG2's output voltage at PCC under various load scenarios.

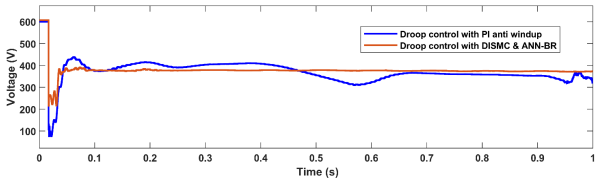

Fig. 17. Load voltage under varying load conditions.

performances are compared.

The output power of PV under variable irradiance levels is shown in Fig. 12. The PV-generated power varies with the change in solar irradiance level. The wind turbine power output at varying wind conditions is shown in Fig. 13. The output power of a

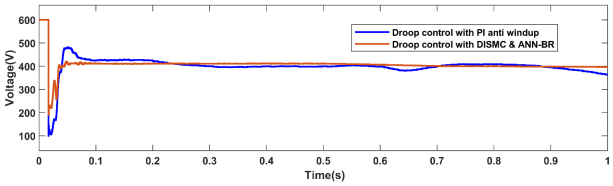

Fig. 18. Frequency at PCC with different loads.

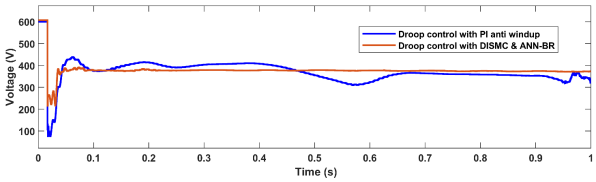

Fig. 19. Frequency share between two DGs using droop control with PI anti-windup.

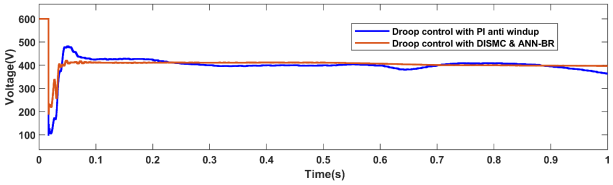

Fig. 20. Frequency share between two DGs using droop control with DISMC and ANN-BR.

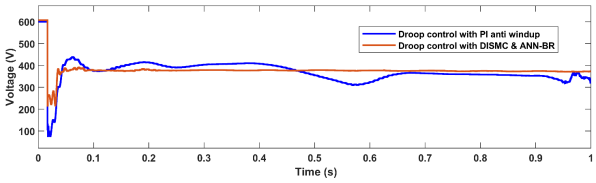

Fig. 21. DG1's output voltage at PCC under various load scenarios.

wind turbine varies from 0 to 0.2sec and minimally varies with time. The fuel cell generated voltage is depicted in Fig. 14. The generated voltage varies minimally with time.

Case study 1: The system working with the combination of energy sources, wind turbine, and BESS fed to inverter 1, PV and wind turbine fed to inverter 2, and fuel cell and BESS fed to inverter 3.

Fig. 15 displays the DG1's output voltage. Despite the variation of renewable energy output power and the load, the output voltage response using droop control with DISMC and ANN-BR initially oscillates and afterward produces stable voltage. This proves that the proposed controller is immune to the load variations. When droop control with a PI anti-windup controller is used, the voltage output deviates from the reference and oscillates, when the load varies. At a light load period, the voltage rises. At time 0.5-0.6sec as the load increases, the output voltage decreases. The controller tries to improve the output voltage but cannot achieve stability. At the final period of 0.9-0.1sec, the load suddenly rises and the voltage is affected in a decreasing manner. The comparison of the voltage characteristics between the proposed controller and droop control with the PI anti-windup controller is shown in Table 3.

Fig. 16 displays the DG2's output voltage. When using droop control with DISMC and ANN-BR, the output voltage drops from the reference and becomes stable thereon. On the other hand droop control with a PI anti-windup controller cannot supply stable voltage when the load changes. Initially, at light load, the output

Table 2. Active and reactive power load variation scenario.

Time (in sec)	P demand (kW)	Q demand (kVar)
0-0.1	4	5
0.1-0.2	6	18
0.2-0.3	10	13
0.3-0.4	6	36
0.4-0.5	16	25
0.5-0.6	50	100
0.6-0.7	8	40
0.7-0.8	5	25
0.8-0.9	16	14
0.9-1	4	20

Table 3. Comparison of the voltage output properties of the suggested and existing controllers.

Controller	Rise time	Slew rate	Overshoot	Undershoot
PI	920.655us	63.195(/ms)	154.182%	104.448%
DISMC and ANN-BR	9.530ms	13.293(/ms)	38.646%	21.741%

voltage rises. At time 0.2sec when the load increases the output voltage decreases below the reference voltage. At 0.5-0.6sec the controller tries to correct the voltage output but in vain. When the load decreases at 0.6-0.9sec the output voltage decreases initially but rises again. It cannot maintain stability. At the final time of 0.8-1sec, the load decreases again. This shows that the PI controller lacks immunity to the larger load variation.

The load voltage comparison between the two controllers is shown in Fig. 17. Using droop control with DISMC and ANN-BR has better results compared to PI anti-windup. The former is capable of supplying the reference voltage with only minimal fluctuation. In the droop control with PI anti-windup, the more the load changes, the more the voltage fluctuates. It is also unable to supply the reference voltage smoothly. It may affect the electrical appliances that are connected to the microgrid. At 0.2-0.6sec, when the load starts gradually increasing, the load voltage decreases. At 0.5-0.6sec peak load period, the load voltage decreases further.

The comparison of frequency between the controllers is shown in Fig. 18 and Table 4. Here also, droop control with DISMC and ANN-BR shows better frequency response in comparison with PI anti-windup. At $t = 0.02 - 0.18$sec, the frequency variation ranges between 49.8Hz and 50.39Hz; then it converges towards the reference value. The frequency shows minimal fluctuation despite large load variation. Whereas, when using droop control with PI anti-windup frequency response is varied. Initially, the frequency falls to 49.6Hz, rises to 50.42Hz at 0.11sec to 0.26sec, and comes to normal and again rises to 50.3Hz when the load varies. The frequency response deviated more, as the load varied.

The frequency share between two DGs using the droop control with PI anti-windup controller is depicted in Fig. 19. It is noticed that unequal sharing of frequency throughout the operation oscillates between 49.7Hz to 50.4Hz. The frequency does not match between the two DGs for most of the period when the load varies. This may shorten the life span of electrical equipment.

The frequency share between two DGs using the droop control with DISMC and ANN-BR controller is shown in Fig. 20. Frequency sharing is most likely equal sharing throughout the operation. It fluctuates only from 49.93Hz to 50.1Hz at 0.55sec to 1sec. The percentage of frequency fluctuation is less compared to the PI controller. The proposed controller has higher synchronization than the PI controller.

Table 4. Comparison of the frequency output characteristics between PI and proposed controllers.

Controllers	Rise time	Settling time	Undershoot
PI	37.770ms	20.281ms	3.684%
DISMC and ANN-BR	25.911ms	19.383ms	1.561%

Table 5. Output voltage comparison between existing and suggested controllers.

Controllers	Settling time	Overshoot
PI	19.285ms	42.253%
DISMC and ANN-BR	13.258ms	24.687%

Case study 2: Operation of the system with the combination energy sources, wind turbine and BESS fed to inverter 1, PV and BESS to inverter 2, and fuel cell and BESS fed to inverter 3.

Fig. 21 depicts the DG1's output voltage. At t=0-0.1sec, the voltage in both controllers is varied. Afterwards, at t =0.1-0.3sec, droop control with DISMC and ANN-BR has stable operation whereas droop control with PI anti-windup has a reduced supply of output voltage as load increases. With droop control with PI anti-windup, when the load fluctuates, the voltage again rises above the reference. At 0.4-0.55sec load increases to maximum, and the voltage drops. The comparison of the voltage characteristics between the proposed controller and droop control with the PI anti-windup controller is shown in Table 5.

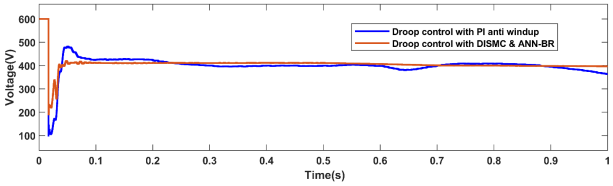

Fig. 22. DG2's output voltage at PCC under various load scenarios.

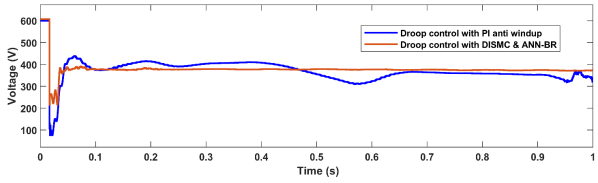

Fig. 23. Load voltage under varying load conditions.

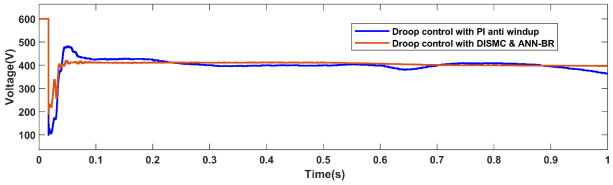

Fig. 24. Frequency at PCC with different loads.

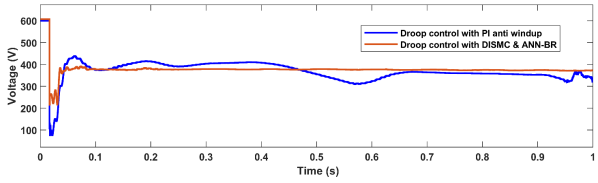

Fig. 25. Frequency share between two DGs sing droop control with PI anti-windup.

Fig. 22 depicts the DG2's output voltage. At t=0-0.1sec, the voltage in both controllers is varied. Droop control with DISMC and ANN-BR has stable operation, it varies marginally at 0.1–0.2sec. It is capable of resisting large load variations whereas

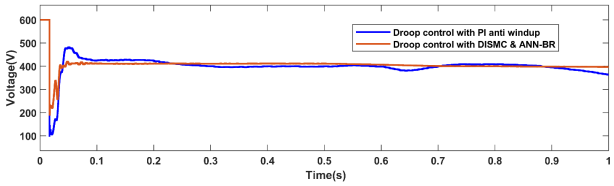

Fig. 26. Frequency share between two DGs sing droop control with DISMC and ANN-BR.

Table 6. Performance comparison between the proposed controller and fuzzy logic [22] under violent load variation.

Parameters	**With fuzzy logic controller [22]**	**Proposed controller**
Maximum value of real power load	20kW	50kW
Maximum value of reactive power	8kVar	100kVar
Fuel cell voltage fluctuation	180-405V	555-565V
Buses frequency fluctuation	Frequently changes the magnitude	Initially fluctuates but afterward stable frequency
Voltage variation	Voltage deep near 200V	Voltage fluctuates initially but afterward stable voltage

droop control with PI anti-windup has a reduced supply of output voltage at 0.1- 0.4sec when the load increases. When the load is increased to a maximum of 0.5- 0.6sec the PI controllers try to maintain a stable voltage but in vain. When the reactive power demand decreases the voltage level is supposed to improve. Instead, it decreases, hence it can't sustain the load fluctuation.

Fig. 23 displays the load voltage comparison. When using DISMC and ANN-BR controllers, the load voltage initially varies at 0-0.2sec. Afterward, the load voltage has a supply reference voltage even though the load varies. It can sustain high load variation except for minimal voltage fluctuation. Whereas, when using droop control with PI anti-windup the large load variation affects the load voltage. The load voltage fluctuates largely throughout the operation. The voltage may have a high chance of containing large harmonics. It may cause more power dissipation in the form of heat and also overheats the connected equipment.

The frequency comparison between the two controllers is depicted in Fig. 24. The frequency with droop control with DISMC and ANN-BR has a rise time of 9.730ms and undershoot of 1.989%. Whereas droop control with PI anti-windup has a value of rise time 57.256ms and undershoot of 2.552% which is greater than controller DISMC and ANN-BR controller. The proposed controller frequency initially rises but afterwards, it tracks the reference value despite load changes. The PI controller deviates when the load changes at 0.1-0.3sec. At light load, the frequency normalizes to the reference value. And also from 0.4-0.53sec when the load increases the frequency drops. But it tries to normalize itself later on. The PI controller frequency response is affected by the loading pattern.

The frequency share between two DGs using the droop control with PI anti-windup controller is depicted in Fig. 25. It is noticed that unequal sharing of frequency throughout the operation oscillates between 49.5Hz to 50.4Hz. At 0.4-0.5sec when the real and reactive power demand increases the frequency drops from the normal but it tries to normalize. The mismatch of frequencies between the two DGs is seen. Moreover, it shows that no equal sharing of load takes place between the two DGs.

The frequency share between two DGs using the droop control with DISMC and ANN-BR controller is shown in Fig. 26. Frequency sharing most likely has equal sharing throughout the operation and fluctuates minimally at 0.55sec to 1sec. Even though the load varies, the frequency response matches between the two DGs. It can be concluded that there is equal sharing of load between the DGs.

To authenticate the work, the proposed controller and fuzzy logic [22] performance under a highly variable load is shown in Table 6.

From the comparison, the proposed model uses a higher load and is observed that the proposed controller can maintain a stable and standard output frequency and voltage than the existing controller defined in [22], even though the higher load varies. The proposed controller is capable of handling only defined loads and disturbances. The addition of more loads to the model affects the output voltages. Voltage drops from the nominal value and the frequency oscillates more due to the controller's incapability to supply higher current demand. It affects the synchronization between the two DG units. Moreover, the renewable energy sources acting as voltage sources vary in nature depending largely on the environmental condition. If the power sources are constant, the performance of the control may get better.

6. CONCLUSION

In this paper, Double Integral Sliding Mode Control (DISMC) and Feed Forward Bayesian Regularization (FF-BR) algorithms are proposed to enhance the performance of droop control. DISMC is designed to control voltage and steady-state error. ANN-BR is trained to regulate current. The energy sources such as the PV, fuel cell, wind turbine power generation systems, and BESS are modeled and implemented in the proposed islanded microgrid. This research work is divided into two cases studies and their results are analyzed. The proposed model is simulated and tested in the Matlab/Simulink environment. The controller offers a few superior performances such as high immunity to load changes, higher accuracy, and tracking precision. Due to these characteristics features, the controller is used in islanded microgrids with high dynamic and sensitive loads to supply quality power. The performance of the proposed controller is tested under time-varying loads. The simulated results conclude that the recommended droop control with DISMC and ANN-BR possesses superior performance and high immunity. It can sustain the nominal frequency and voltage of the microgrid under tremendously varying loads. In the future, this work will extend to design a better controller to handle more dynamic and sensitive loads for the islanded microgrid. Moreover, this work will extend near to the actual microgrid model.

REFERENCES

[1] G. De Vanna, M. Longo, F. Foiadelli, M. Panteli, and M. Galeela, "Reliability and resilience analysis and comparison of off-grid microgrids," in *2020 55th Int. Univ. Power Eng. Conf.*, pp. 1–6, IEEE, 2020.

[2] K. Matharani and H. Jariwala, "Stability analysis of microgrid with passive, active, and dynamic load," *J. Oper. Autom. Power Eng.*, vol. 11, no. 4, pp. 295–306, 2023.

[3] P. Arul, V. K. Ramachandaramurthy, and R. Rajkumar, "Control strategies for a hybrid renewable energy system: A review," *Renewable Sustainable Energy Rev.*, vol. 42, pp. 597–608, 2015.

[4] H. Karimi-Davijani and O. Ojo, "Dynamic operation and control of a multi-dg unit standalone microgrid," in *ISGT 2011*, pp. 1–7, IEEE, 2011.

[5] H. Bevrani, M. Watanabe, and Y. Mitani, "Micro-grid controls, standard handbook for electrical engineers," in *in Sect. 16, 16th Ed. In: Wayne Beaty H, editor. New York: McGraw Hill, USA*, pp. 160–176, IEEE, 2012.

[6] H. Bevrani and S. Shokoohi, "An intelligent droop control for simultaneous voltage and frequency regulation in islanded microgrids," *IEEE Trans. Smart Grid*, vol. 4, no. 3, pp. 1505–1513, 2013.

[7] H. Shayeghi and A. Rahnama, "Frequency regulation of a standalone interconnected ac microgrid using innovative

multistage tdf (1+ fopi) controller," *J. Oper. Autom. Power Eng.*, vol. 12, no. 2, pp. 121–133, 2024.

[8] M. Gholami, A. Pisano, S. M. Hosseini, and E. Usai, "Distributed finite-time secondary control of islanded microgrids by coupled sliding-mode technique," in *2020 25th IEEE Int. Conf. Emerging Technol. Factory Autom.*, vol. 1, pp. 454–461, IEEE, 2020.

[9] J. M. Guerrero, J. C. Vasquez, J. Matas, L. G. De Vicuña, and M. Castilla, "Hierarchical control of droop-controlled ac and dc microgrids—a general approach toward standardization," *IEEE Trans. Ind. Electron.*, vol. 58, no. 1, pp. 158–172, 2010.

[10] B. Ning, Q.-L. Han, and L. Ding, "Distributed secondary control of ac microgrids with external disturbances and directed communication topologies: A full-order sliding-mode approach," *IEEE/CAA J. Autom. Sin.*, vol. 8, no. 3, pp. 554–564, 2020.

[11] S. Ullah, L. Khan, I. Sami, and J.-S. Ro, "Voltage/frequency regulation with optimal load dispatch in microgrids using smc based distributed cooperative control," *IEEE Access*, vol. 10, pp. 64873–64889, 2022.

[12] M. Jafari, V. Sarfi, A. Ghasemkhani, H. Livani, L. Yang, H. Xu, and R. Koosha, "Adaptive neural network based intelligent secondary control for microgrids," in *2018 IEEE Texas Power Energy Conf.*, pp. 1–6, IEEE, 2018.

[13] S. Shokoohi, S. Golshannavaz, R. Khezri, and H. Bevrani, "Intelligent secondary control in smart microgrids: an on-line approach for islanded operations," *Optim. Eng.*, vol. 19, pp. 917–936, 2018.

[14] N. M. Dehkordi, H. R. Baghaee, N. Sadati, and J. M. Guerrero, "Distributed noise-resilient secondary voltage and frequency control for islanded microgrids," *IEEE Trans. Smart Grid*, vol. 10, no. 4, pp. 3780–3790, 2018.

[15] E. Sohrabzadi, M. Gheisarnejad, Z. Esfahani, and M. H. Khooban, "A novel intelligent ultra-local model control-based type-ii fuzzy for frequency regulation of multi-microgrids," *Trans. Inst. Meas. Control*, vol. 44, no. 5, pp. 1134–1148, 2022.

[16] N.-L. Mo, Z.-H. Guan, D.-X. Zhang, X.-M. Cheng, Z.-W. Liu, and T. Li, "Data-driven based optimal distributed frequency control for islanded ac microgrids," *Int. J. Electr. Power Energy Syst.*, vol. 119, p. 105904, 2020.

[17] J. Liu, Q. Yao, and Y. Hu, "Model predictive control for load frequency of hybrid power system with wind power and thermal power," *Energy*, vol. 172, pp. 555–565, 2019.

[18] J. Pahasa and I. Ngamroo, "Coordinated control of wind turbine blade pitch angle and phevs using mpcs for load frequency control of microgrid," *IEEE Syst. J.*, vol. 10, no. 1, pp. 97–105, 2014.

[19] S. K. Pandey, S. R. Mohanty, N. Kishor, and J. P. Catalão, "Frequency regulation in hybrid power systems using particle swarm optimization and linear matrix inequalities based robust controller design," *Int. J. Electr. Power Energy Syst.*, vol. 63, pp. 887–900, 2014.

[20] A. A. El-Fergany and M. A. El-Hameed, "Efficient frequency controllers for autonomous two-area hybrid microgrid system using social-spider optimiser," *IET Gener. Transm. Distrib.*, vol. 11, no. 3, pp. 637–648, 2017.

[21] J. Guo, "Application of full order sliding mode control based on different areas power system with load frequency control," *ISA Trans.*, vol. 92, pp. 23–34, 2019.

[22] S. Roozbehani, M. T. Hagh, and S. G. Zadeh, "Frequency control of islanded wind-powered microgrid based on coordinated robust dynamic droop power sharing," *IET Gener. Transm. Distrib.*, vol. 13, no. 21, pp. 4968–4977, 2019.

[23] T. Vigneysh and N. Kumarappan, "Autonomous operation and control of photovoltaic/solid oxide fuel cell/battery energy storage based microgrid using fuzzy logic controller," *Int. J. Hydrogen Energy*, vol. 41, no. 3, pp. 1877–1891, 2016.

[24] T.-C. Ou and C.-M. Hong, "Dynamic operation and control of microgrid hybrid power systems," *Energy*, vol. 66, pp. 314–323, 2014.

[25] W.-M. Lin, C.-M. Hong, C.-H. Huang, and T.-C. Ou, "Hybrid control of a wind induction generator based on grey–elman neural network," *IEEE Trans. Control Syst. Technol.*, vol. 21, no. 6, pp. 2367–2373, 2013.

[26] J.-H. Jung, S. Ahmed, and P. Enjeti, "Pem fuel cell stack model development for real-time simulation applications," *IEEE Trans. Ind. Electron.*, vol. 58, no. 9, pp. 4217–4231, 2010.

[27] T.-C. Ou and C.-M. Hong, "Dynamic operation and control of microgrid hybrid power systems," *Energy*, vol. 66, pp. 314–323, 2014.

[28] T. Vigneysh and N. Kumarappan, "Artificial neural network based droop-control technique for accurate power sharing in an islanded microgrid," *Int. J. Comput. Intell. Syst.*, vol. 9, no. 5, pp. 827–838, 2016.

[29] S. Ahmadi, S. Shokoohi, and H. Bevrani, "A fuzzy logic-based droop control for simultaneous voltage and frequency regulation in an ac microgrid," *Int. J. Electr. Power Energy Syst.*, vol. 64, pp. 148–155, 2015.

[30] A. Alahmad, A. Saffarian, S. Seifossadat, and S. Mortazavi, "Frequency and voltage stability of the islanded microgrid with multi dc-bus based-inverter using droop control," *J. Oper. Autom. Power Eng.*, 2023.

[31] S.-C. Chen and C.-Y. Kuo, "Design and implementation of double-integral sliding-mode controller for brushless direct current motor speed control," *Adv. Mech. Eng.*, vol. 9, no. 11, p. 1687814017737724, 2017.

[32] P. Tahmasebi and A. Hezarkhani, "Application of a modular feedforward neural network for grade estimation," *Nat. Resour. Res.*, vol. 20, pp. 25–32, 2011.

[33] A. Sadighi, *Artificial Intelligence to Determine Sulfate Solubility*. PhD thesis, 10 2021.